Insights into the 3D structure and behaviour of Icelandic crystal mushes from gabbroic nodules

Rahul Subbaraman[1,*], Margaret E. Hartley[1], Jonathan Fellowes[1], Margherita Polacci[1], Barbara Bonechi[1], Lucia Pappalardo[2], Gianmarco Buono[2], David A. Neave[1]

[1] Department of Earth and Environmental Sciences, University of Manchester, Oxford Road, Manchester, M13 9PL, UK

[2] Istituto Nazionale di Geofisica e Vulcanologia – Osservatorio Vesuviano, Via Diocleziano 328, 80125 Napoli, Italy

Corresponding author: Rahul Subbaraman
rahul.subbaraman@manchester.ac.uk

This article has been peer-reviewed and accepted for publication in *Earth and Planetary Science Letters*. The final version of record is currently in production and will be available from the publisher with a DOI shortly.

Insights into the 3D structure and behaviour of Icelandic crystal mushes from gabbroic nodules

Rahul Subbaraman[a], Margaret E. Hartley[a], Jonathan Fellowes[a], Margherita Polacci[a], Barbara Bonechi[a], Lucia Pappalardo[b], Gianmarco Buono[b], David A. Neave[a]

[a]*Department of Earth and Environmental Sciences, University of Manchester, Oxford Road, Manchester, M13 9PL, UK*
[b]*Istituto Nazionale di Geofisica e Vulcanologia - Osservatorio Vesuviano - Sezione di Napoli, Via Diocleziano, 328, 80125, Napoli NA, Italy*

Abstract

Crystal mushes – porous yet cohesive frameworks of crystals interspersed with interstitial melts – form the plumbing systems of most active volcanoes. In Iceland, magmatic plumbing systems are inferred to be constructed from vertically stacked mushy magma reservoirs separated by subsolidus rock. Gabbroic nodules from Gígöldur in central Iceland provide a rare window into the structure, evolution, and degassing behaviour of upper crustal (6–10 km) mushy magma reservoirs. These plagioclase-rich nodules preserve recycled high-An plagioclase cores, rim overgrowths, and interstitial crystallisation of mafic phases, reflecting *in situ* modification within the final storage reservoir and roof cumulate formation via density-driven segregation. Oscillatory zoning and variable rim patterns indicate that crystals experienced non-steady-state growth and were incorporated into clusters at different times. Compositional similarities between carrier and interstitial melts demonstrate that the final stages of mush evolution occurred in relatively homogeneous melts. Volatile saturation pressures of ~2.0–2.8 kbar, together with high vesicularities (21–30 vol.%) and extensive connectivities (>93%), are con-

sistent with the presence of a CO_2-rich vapour phase within the mush. Nodules are erupted when a rigid crystal framework and a well-connected bubble network that enables effective degassing, preserve their integrity. When bubble networks fail to form, degassing disrupts the framework – even if initially rigid – causing disaggregation into plagioclase-phyric crystal cargoes, akin to plagioclase-ultraphyric basalts erupted in diverse settings. Nodules record the dynamics of stratified mushy magma reservoirs, the influence of volatiles on mush behaviour, and the transport of crystalline material in active volcanic systems, providing key insights into how crystal mushes shape the storage and mobilisation of magma in the Earth's crust.
Keywords: gabbroic nodules, crystal mush, magma plumbing system, plagioclase-rich cumulates, stratified magma reservoirs, Icelandic volcanism

1. Introduction

Active volcanoes in many settings are increasingly understood to be fed from geometrically complex transcrustal plumbing systems composed of crystal mushes – cohesive yet porous frameworks of crystals interspersed with interstitial melts (e.g., Annen et al., 2005; Edmonds et al., 2019). Plumbing systems are often discussed in terms of two endmember architectures. In continental settings, plumbing systems are typically described as largely continuous mush columns that extend through much of the crust (e.g., Cashman et al., 2017; Paulatto et al., 2019), whereas in oceanic settings such as Iceland, they are often depicted as stacked, localised mushy magma reservoirs that are dispersed through the crust but separated by melt-free country rock (e.g., Chamberlain et al., 2019; Maclennan, 2019). In this stacked-sill configuration, mush zones form at the margins of individual sills

emplaced into subsolidus crust, reflecting localised rather than pervasive mush development (Maclennan, 2019). Examining the pre- and syn-eruptive textures of crystal mushes in 3D can constrain the conditions and dynamics of magma storage, remobilisation, and ascent, thereby helping to refine models of magma behaviour (e.g., Bergantz et al., 2015; Sparks and Cashman, 2017; Humphreys et al., 2025). However, this undertaking is extremely challenging. Mush-derived clots of crystals often lose their spatial contexts by disaggregation during magma ascent (e.g., Hansen and Grönvold, 2000; Holness et al., 2007; Lange et al., 2013), while mushes preserved in fossil magma reservoirs are subject to overprinting by post-emplacement physical and chemical processes (e.g., O'Driscoll et al., 2010; Holness et al., 2017). In this context, gabbroic nodules, also known as cognate xenoliths, plutonic nodules, or crystalline enclaves (Holness et al., 2019), presents vital opportunities to investigate the petrology of mushy magma reservoirs beneath basaltic volcanoes. While numerous studies have explored the 2D structure of mush fragments and mush-derived crystal clusters in basalts (e.g., Neave et al., 2014b; Horn et al., 2022; Holness et al., 2019), analogous 3D studies remain to be undertaken. Such 3D imaging provides a more comprehensive view of nodule textures by capturing geometric and spatial relationships that are difficult (or sometimes impossible) to interpret from 2D sections alone. In particular, 3D data can reveal vesicle size distributions and connectivity (Polacci et al., 2009; Bamber et al., 2024) – features that inform interpretations of degassing pathways and deformation history – as well as the spatial arrangement and interconnectivity of crystalline frameworks and interstitial phases. These insights are commonly obscured or misrepresented in 2D due to sectioning bias (e.g., Mangler et al., 2022).

Constraining the distribution and behaviour of H_2O and CO_2 in crystal mushes is essential for deciphering their degassing behaviour within magma plumbing systems and their influence on magma ascent dynamics and crystal mush disaggregation (e.g., Edmonds and Wallace, 2017). As volatiles exsolve, they form bubbles that, when preserved, become vesicles and provide vital clues about degassing processes. Studying vesicle textures is therefore a key approach to reconstructing volatile behaviour in magma systems. Advances in X-ray computed microtomography (XCT), pioneered by Proussevitch et al. (1998), have revolutionised vesicle studies, offering insights into outgassing dynamics, bubble coalescence, and magma ascent behaviour during eruptions. A deeper understanding of these processes improves our ability to interpret magma degassing pathways, pressure changes, and fragmentation dynamics. In turn, these factors directly influence eruption style, intensity, and timing (Klug and Cashman, 1994; Cashman and Mangan, 2014), with direct implications for enhancing predictions of eruptive behaviour and informing volcanic hazard mitigation. Vesicle size distributions are widely used to infer nucleation, growth, and coalescence events during vesiculation (Klug and Cashman, 1994). X-ray computed microtomography (XCT) analyses of volcanic samples from Ambrym (Vanuatu), Hunga Tonga-Hunga Ha'apa (Tonga), and Las Sierras-Masaya (Nicaragua), as well as several Italian volcanoes including Etna, Somma–Vesuvius, Campi Flegrei, and Stromboli, and La Palma (Canary Islands, Spain), have demonstrated the utility of this technique in tracking vesicle connectivity and vesicle number density in pyroclasts (Polacci et al., 2009, 2012; Colombier et al., 2018; Pappalardo et al., 2018; Liedl et al., 2019; Bamber et al., 2024; Bonechi et al., 2025). Vesicle connectivity provides a measure of gas escape efficiency through permeable bubble networks, while vesicle number den-

sity can reflect volatile nucleation and decompression rates. Together they offer critical insights into magma degassing, ascent dynamics, and eruptive style, including whether magma undergoes explosive fragmentation or degasses passively (e.g., Klug and Cashman, 1996; Toramaru, 2006; Shea et al., 2010).

While XCT approaches are typically applied to tephra, applying the same principles to gabbroic nodules offers a unique opportunity to investigate degassing in a contrasting environment – one where a rigid crystal framework coexists with an exsolving volatile phase. Exsolved volatiles reduce magma density and aid ascent, but if bubble growth and overpressure are not efficiently relieved through gas or melt escape, they can generate stresses that cause nodule disaggregation, as observed in mafic enclaves within volcanic rocks (e.g., Bacon, 1986; Candela, 1991). Understanding mush disaggregation also raises important questions about how crystal mush fragments become entrained, transported and preserved during magma ascent. The detachment of such fragments, likely driven by fracturing and dislodgement from their source regions, remains poorly understood (Holness et al., 2019). To survive transport without breaking down into isolated macrocrysts (e.g., Hansen and Grönvold, 2000; Lange et al., 2013; Neave et al., 2014b), entrained mush fragments must retain sufficient structural integrity. Most erupted nodules contain >60 vol.% crystals and <30 vol.% vesicles (Holness et al., 2019), reflecting the minimum crystal fraction required to form a mechanically stable framework and the weakening effects of increasing vesicularity (Coombs et al., 2003).

Here, we focus on exceptionally well-preserved gabbroic nodules from Gígöldur in central Iceland, first reported by Hansen and Grönvold (2000). These nodules

consist of a rigid crystal framework, interstitial melt, and vesicles, forming a naturally preserved three-phase system that retains critical information about mush structure and ascent behaviour. We use these nodules to address two key questions: (1) What factors control whether gabbroic nodules retain their structural integrity or undergo disaggregation during ascent? (2) What processes govern the formation and evolution of mushes beneath Gígöldur? By addressing these questions, we show that gabbroic nodules provide a valuable archive for reconstructing crystal mush dynamics and the conditions that govern disaggregation, offering insights into how such processes influence magma storage, transport and eruption in volcanic systems globally.

2. Samples and analytical methods

Gígöldur is a broad NNE-SSW-trending ridge of interlayered hyaloclastites and craters situated in the highlands north of Vatnajökull glacier, located between Bárðarbunga to the southwest and Askja to the northeast (Figure 1a; Hansen and Grönvold, 2000). Nodule samples were collected from two locations along the ridge, approximately 5 km apart, referred to as Gígöldur Central and Gígöldur South (Figure 1b,c). The nodules are 5–10 cm in diameter, rounded to sub-angular, and composed mainly of plagioclase aggregates encased in glass. They also contain small but variable amounts of interstitial olivine, and interstitial dark green clinopyroxene is present in some nodules. They exhibit high vesicularity and significant textural and mineralogical variability (Figure 1d). While most nodules were picked up loose from the float, some nodules were found *in situ* within plagioclase-phyric scoriaceous agglutinates (Figure 1e,f).

A summary of samples analysed in this study, including sample types and the analytical techniques used, is provided in Supplementary Table B1. Two nodules (GO19-01a.X and GO19-02.X), each about 10 cm in their longest dimension (Figure 1g) but relatively thin (~3 cm), were selected for further investigation because their thin geometries allowed the XCT scan cores to encompass a substantial proportion of the total nodule volumes. Four cylindrical rock cores were drilled from each nodule (Figure 1h). These cores are named C1–C4, respectively. The cores are 15 mm in diameter and 16.7 to 27.5 mm in height to accommodate variations in nodule morphologies while maintaining sample integrity. Cores from sample GO19-01a.X were designated Batch I, and those from GO19-02.X were designated Batch II, corresponding to their nodule of origin. Because the two samples responded differently to X-ray exposure, different exposure times were required, which in turn necessitated slightly different segmentation strategies. A total of seven thin sections were prepared from areas between the cores of both nodules.

Plane-polarised light (PPL) images were captured at a high resolution of 5000 pixels per inch using a GX Microscopes PrimeScan system. Partial-XPL (PXPL; polariser–analyser 45°) and XPL (90°) images were acquired at ×10 magnification using a uScope GX-1020 Geological Slide Scanner; the PXPL setup avoids complete extinction of silicate phases across thin sections without access to circular polarisation. Phase proportions were quantified through a modified point-counting method using the image analysis software JMicroVision v. 1.3.4 (Roduit, 2008). PPL or PXPL images of the thin sections were systematically segmented into equal-area rectangles. Successive grids were generated by subdividing the initial grid at its midpoints, enabling a detailed assessment of mineral distribution

and precise quantification of all constituent phases across the thin sections.

X-ray computed microtomography (XCT) was performed using a Carl Zeiss Xradia Versa-410 3D X-ray microscope at the Istituto Nazionale di Geofisica e Vulcanologia - Sezione di Napoli Osservatorio Vesuviano (INGV-OV), Naples, Italy. Scans were performed in absorption mode with 1601 projections collected over a 360° rotation at 90 kV and 8 W, and an optical magnification of ×0.4, resulting in a nominal voxel size of 16.0918 µm. Typical macrocrysts are ≥100 µm in length, and the smallest interstitial melt films between them are at least 20 µm thick, while most bubbles have minimum dimensions of ≥10 µm. Thus, our voxel size is sufficient to resolve the textural features relevant to our goals. Data were reconstructed using XRMReconstructor, and vesicle and crystal geometries were characterised and quantified using Thermo Scientific™ Avizo v. 2019.1 and Fiji v1.54f. Details of the XCT analysis methods are provided in the supplementary material. The raw files are provided in Subbaraman et al. (2025a). Our XCT analysis aimed to distinguish constituent phases – plagioclase, olivine, clinopyroxene, matrix glass, and vesicles – using a lab-based XCT setup. However, since we used absorption contrast mode and prioritised glass-plagioclase separation, olivine and clinopyroxene could not be distinguished in Batch I, necessitating their combined classification as mafics in subsequent analyses and discussions.

Minerals and glasses were geochemically characterised in one representative thin section from each of the scanned nodules (GO19-01a.6 and GO19-02.4; Supplementary Table B1). These thin sections were selected to minimise the presence of ash within vesicles (to avoid complications in density calculations) while ensuring

that all major phases were included. Additional mineral analyses were conducted on five additional nodule thin sections and three scoria thin sections, representing different sampling locations and textures to capture mineralogical variability. Glass analyses were performed on four nodule and two scoria thin sections from this set. Major and minor element compositions of minerals and interstitial glass were determined by electron probe microanalysis (EPMA) on a Cameca SX100 instrument at the Williamson Research Centre, University of Manchester. Analyses were performed under typical operating conditions of 15 kV accelerating voltage, 5–40 nA beam current, and 1–10 μm beam diameter, with counting times of 20–60 s on-peak and 10–30 s off-peak depending on the phase. Accuracy and precision were monitored using secondary standards. Detection limits for individual oxides were typically: SiO_2, MgO, FeO, Al_2O_3, CaO ~0.03–0.04 wt%; MnO, TiO_2, NiO ~0.04–0.06 wt%; and Cr_2O_3, Na_2O, K_2O, P_2O_5 ~0.01–0.02 wt%. Full details of analytical setups, standard measurements, and instrument configurations are provided in the supplementary material.

Magmatic H_2O concentrations were reconstructed from published melt inclusion data. We compiled clinopyroxene-, olivine-, and plagioclase-hosted melt inclusions from Holuhraun (Bali et al., 2018), together with olivine-hosted inclusions from Skuggafjöll (Neave et al., 2014b), comprising a total of 209 melt inclusions (see supplementary material). These two systems were selected because they are geographically close to, and geochemically comparable with, Gígöldur (Supplementary Figure B1). Within this combined dataset, melt inclusions define a coherent linear relationship between MgO and H_2O (Supplementary Figure B2). Because Ce data (commonly used as a proxy for H_2O under H_2O-undersaturated

conditions) are unavailable for Gígöldur, this MgO-H_2O correlation provides the basis for reconstructing magmatic H_2O concentrations in the Gígöldur lavas.

Plausible CO_2 concentrations were reconstructed from maximum CO_2/Ba ratios in a dataset comprising 336 clinopyroxene-hosted, olivine-hosted, and plagioclase-hosted melt inclusions from Borgarhraun, Holuhraun, and Skuggafjöll (Supplementary Table B4; full data in the supplementary material; Hauri et al., 2017; Bali et al., 2018; Neave et al., 2014a). CO_2/Ba ratios were converted to CO_2 concentrations using the Ba content of Gígöldur nodule glass (19 ppm; Hansen and Grönvold, 2000). For each locality and host phase, *realistic maximum* CO_2 values were calculated using the Tukey upper bound (Q3 + 1.5 × IQR; Tukey, 1977) of the CO_2/Ba distributions to provide conservative upper limits while minimising the influence of extreme outliers.

Storage conditions were constrained with the empirical olivine–plagioclase–augite–melt (OPAM) thermobarometer of Higgins and Stock (2024), which applies a multivariate regression to melt major element chemistry (matrix glasses here) and a statistical filter that evaluates the probability of OPAM saturation. We retain only high-probability OPAM-saturated solutions (low-probability/edge-of-calibration cases are rejected; thresholding details in Higgins and Stock, 2024). The calibration yields standard errors of ±1.14 kbar and ±36 °C, with low systematic uncertainties that are independent of melt H_2O.

Bulk nodule densities were determined by combining modal mineral proportions from point counting with mineral and interstitial melt densities, both calculated

at the inferred P–T conditions of magma storage. Melt densities were obtained using a partial molar volume approach following Lange and Carmichael (1990), in which oxide contributions vary with pressure and temperature. Mineral densities were calculated from their endmember compositions and the thermoelastic formulation of Berman (1988), which accounts for P–T effects on molar volumes. To assess the buoyancy of the nodules, carrier melt (scoria matrix glass) densities were also calculated at the same P–T. The procedures for liquid and mineral density calculations, including the equations and thermodynamic parameters used, are detailed in the supplementary material, and the Python code is available at **?**.

3. Results

3.1. Petrography and point counting

Point counting (~3400 points per section) shows that the nodules are strongly plagioclase-dominated (50–64 vol%). Olivine ranges from 0.7–4.2 vol% when clinopyroxene is present (2.8–9.8 vol%) and 1.9–8.5 vol% when it is absent. Interstitial glass makes up 8.6–20.7 vol%, and vesicles 16–25 vol% (Figure 2a). These proportions place the nodules within the IUGS fields of anorthosite, leucotroctolite, and leuco-gabbro (Figure 2b). All samples contain plagioclase, olivine, glass, and vesicles; clinopyroxene is restricted to GO19-01a.X and GO19-01a.1. Accessory Cr-spinel occurs in GO19-02.X, GO19-01a.1, GO19-01a.3, and GO23-04.N3C, while particulate volcanic ash is confined to vesicle cavities and margins in GO19-02.2. Full thin section photomicrographs are provided in Figure 3a–d.

Plagioclase grains (100 μm to >5 mm) primarily form clusters rather than isolated crystals and often host melt inclusions. XPL photomicrographs reveal multiple

compositional bands enclosing both individual plagioclase crystals and clusters (Figure 3e–j). Olivine grains are typically smaller (<1.5 mm) and are found interstitially between plagioclase clusters, often in the vicinity of vesicles. Clinopyroxene, when present, is subhedral to sub-rounded, enclosed by plagioclase, and contains fractures and melt inclusions. Cr-spinel, when present, is associated with plagioclase and olivine. Vesicles in all samples span a wide range of sizes and degrees of coalescence, from smaller (<0.2 mm) circular vesicles to larger (>1 mm) irregular vesicles that are partially or fully coalesced. They are commonly rimmed by glass of variable thickness. A full set of thin section scans is available in Subbaraman et al. (2025b).

3.2. X-ray computed microtomography (XCT) analysis

In Batch I, vesicles were readily segmented from surrounding glass and crystals using simple thresholding, complemented by image processing techniques in Avizo, including Erosion, Dilation, and Removal of Small Spots. Segmentation in Batch II was more challenging due to a few vesicles containing particulate volcanic ash, which may have caused a slight underestimation of vesicle abundance. Approximately 1 vol.% of pixels in Batch I and 4 vol.% in Batch II remained unassigned due to segmentation limitations. Individual plagioclase crystals show minimal phase contrast with neighbouring grains, so individual plagioclase grains within clusters could not be segmented in either batch. Volumetric proportions from XCT data are shown in Figure 2a, with representative 3D renderings in Figure 4a, b. A full set of reconstructions is available in Subbaraman et al. (2025c).

3.2.1. Minerals and glasses

Mineralogical diversity across the cores, highlighted through 3D visualisation, is detailed in Supplementary Table B3. Estimated volume proportions broadly agree with the point-counting results considering sectioning effects, and highlight systematic differences between the two nodules (Figure 2a). Batch I cores contain 55–60 vol% plagioclase, 4.7–10 vol% mafics, 5.3–9.2 vol% glass, and 25–30 vol% vesicles, whereas Batch II cores contains slightly less plagioclase (50–56 vol%), fewer mafics (4.0–6.5 vol%), more glass (13–20 vol%), and vesicles (22–24 vol%). Accessory Cr-spinel (0.05–0.08 vol%) occurs only in Batch II. Mafic phases occupy interstitial spaces between plagioclase clusters, and are relatively larger and clustered in Batch I, and relatively smaller and more disseminated in Batch II. Apparent clustering of mafic phases most likely reflects the limited resolution of segmentation at grain boundaries. Coarse plagioclase grains in contact could not be reliably separated, precluding quantitative shape analysis.

3.2.2. Vesicles

After applying geometrical filters, 3D volume analysis reveals vesicle sizes spanning approximately 10^4 μm^3 (the conservative lower detection limit imposed by the 16 μm voxel size) to over 10^{10} μm^3 (Supplementary Table B4). Vesicles smaller than the minimum threshold may be present but cannot be robustly identified. Vesicle textures show consistent differences between the two batches, although variability within each batch is comparatively low. Batch I cores have a mean vesicle content of ~27 vol.%, while Batch II cores contain ~22.5 vol.% vesicles. Vesicle connectivity, defined as the volume fraction of interconnected vesicles extending to the core edges, is high across all samples (93.3–98.8%; Supplementary Table B4; Figure 4c). Cores with the highest and lowest connectivity are highlighted in

Figure 4d, illustrating the range of vesicle network development. Vesicles larger than 10^6 μm^3 (constituting >99% of the vesicle volume) are the main focus of subsequent analyses, as smaller vesicles likely formed during syn-eruptive vesiculation in shallow conduits (Klug and Cashman, 1996) and are not directly relevant to mush textures. Large vesicles instead record pre-eruptive bubble growth in magma chambers (Sparks and Brazier, 1982) or syn-eruptive coalescence (Klug and Cashman, 1994).

Vesicle populations exhibit three broad morphological styles that recur across cores: (i) nearly spherical to weakly ellipsoidal vesicles with little or no evidence of coalescence; (ii) sub-spherical to botryoidal vesicles; and (iii) large, irregular and tortuous vesicles formed by partial to extensive coalescence around the crystal framework. These morphologies are consistent with those reported from 2D vesicle textures, but are here fully resolved in 3D. For quantitative analysis, vesicle size distributions (VSDs) were fitted using fixed log-volume bins of 10^6–10^8, 10^8–10^9, and 10^9–10^{10} μm^3 (Figure 5, Supplementary Figure B3). This binning captures the natural breaks in the VSDs across all cores and allows direct comparison between batches (Polacci et al., 2009). The smallest vesicles (10^6–10^8 μm^3) follow power-law distributions with exponents of 0.39–0.44 in Batch I and 0.64–0.74 in Batch II. Medium vesicles (10^8–10^9 μm^3) show power-law trends with exponents 1.04–1.19 in Batch I and 0.44–0.69 in Batch II. The largest vesicles (10^9–10^{10} μm^3) mostly adhere to power-law distributions with exponents of 1.36–1.85 in Batch I and 1.36–1.57 in Batch II (Figure 5). In some cases, they instead exhibit exponential tails, shown by the red curves and annotations in Supplementary Figure B3.

3.3. Storage conditions and volatile contents

Matrix glasses in all nodules and scoria samples are basaltic in composition (Supplementary Figure B3), with nodule matrix glasses chemically similar to scoria matrix glasses (Supplementary Figure B4). OPAM thermobarometry (Higgins and Stock, 2024) indicates that the most probable storage conditions were ~2.45 ± 1.14 kbar and 1211 ± 36°C (Figure 5); calculated phase densities at these conditions are reported in Table 1. Melt inclusion data from Holuhraun and Skuggafjöll, selected for their geochemical similarity to Gígöldur, yield reconstructed H_2O concentrations of approximately 0.30–0.47 wt% (Supplementary Material), based on the observed best-fit linear correlation $H_2O = 0.0520 \times MgO$ (Supplementary Figure B2). For CO_2, the literature compilation of 336 melt inclusions from Borgarhraun, Holuhraun, and Skuggafjöll yields maximum CO_2/Ba ratios of 79–115. Using the Ba content of Gígöldur nodule glass (19 ppm; Hansen and Grönvold, 2000), we estimate a realistic maximum CO_2 concentration of 1120–1350 ppm at depth (Supplementary Table B4).

4. Discussion

4.1. What factors control whether gabbroic nodules retain their structural integrity or undergo disaggregation during ascent?

The absence of obvious fabrics, such as foliation or lineation (Figure 3a-d), together with the near-continuous nature of the plagioclase-dominated framework (~99% in contact), indicates that the crystal frameworks in our samples were stable during eruption. Both 2D and 3D observations suggest that plagioclase grains are dominantly equant to sub-equant, i.e., of low aspect ratio. Indeed, such grain shapes are far less susceptible to bending or fracture during rapid vesicle expansion

than tabular plagioclase (Martin et al., 2006). Moreover, the framework is marked by extensive grain-grain contacts (Figure 3e,f,i), consistent with other melt-bearing rocks in which synneusis reduces melt-wetted boundaries and generates unusually large solid-solid interfaces. Such large contacts strengthen mush cohesion and provide mechanical robustness against disruption during vesicle growth, coalescence, or melt extraction (Holness, 2018). Taken together, these features indicate that the Gígöldur nodules developed a resilient framework capable of withstanding stresses associated with vesiculation and degassing.

The potential for mush framework disruption is strongly influenced by bubble growth and coalescence. Bubble expansion exerts localised stresses on the surrounding crystal network, and extensive bubble coalescence can compromise framework integrity (e.g., Coombs et al., 2003). Combined with the rigid, well-connected plagioclase framework described above, the observed high connectivity in both matrix glasses (>90%) and vesicles (>93%) suggests that gas and melt could escape efficiently while maintaining mechanical stability at least during the final stages of eruption. Vesicle size distributions (Figure 6a, Supplementary Figure B3) provide further insights; the largest vesicles display high power-law exponents (>1), indicative of bubble coalescence facilitating the formation of interconnected degassing pathways (e.g., Gaonac'h et al., 1996; Bai et al., 2008), while exponential fits in some cores (Supplementary Figure B3) suggest that degassing approached near-equilibrium conditions (Bai et al., 2008).

We performed closed-system degassing calcualtions for CO_2, H_2O, and total volatiles in 100 pressure decrements from the depth of final storage (1.67—3.00 kbar) to a

confining pressure of 84.5 bar (~940 m of ice cover, corresponding to the average in central Iceland during the Last Glacial Maximum; Hubbard et al., 2006), using the volatile degassing model of Iacono-Marziano et al. (2012) implemented in the VESIcal Python package (Iacovino et al., 2021). Our calculations (Figure 6b; Supplementary Figure B4) indicate that CO_2 and H_2O exsolve continuously but minimally during ascent through much of the crust, with the majority of exsolution occurring within the uppermost few hundred metres. Bubble growth during ascent exerts stress on the crystal framework, and high volatile contents increase bubble number density, enhancing coalescence and promoting partial disaggregation. Our 3D vesicle analysis and degassing calculations show that framework disaggregation occurred primarily within the uppermost levels of ascent, where bubbles grow and coalesce to volumes sufficient to disrupt the well-connected, equant to sub-equant plagioclase network. Bubbles already present at the final pressure of magma storage (~2.5 kbar) initially have little mechanical effect on the crystal framework, but contribute to stress as they expand during magma ascent.

Our observations are consistent with established models of shallow magma degassing (Degruyter et al., 2019), which identify three primary mechanisms for gas escape: (1) *bubble and crystal suspension* (e.g., Parmigiani et al., 2016) at very high melt fractions (green field in Figure 6c); (2) *volatile channel formation* (e.g., Parmigiani et al., 2011) at moderate melt and high crystal fractions (blue field); and (3) *capillary fracturing* (e.g., Parmigiani et al., 2017) at very low melt fractions, when melt pools are isolated (purple field). At the final storage depth, where the volatile fraction is negligible, and the crystal fraction is expected to be high with isolated interstitial melt pockets, the mush is likely to degas predominantly by cap-

illary fracturing. Indeed, all Gígöldur samples (rock cores and thin sections) plot within this field (triangles in Figure 6c) if vesicles are excluded from their phase proportions. By the time the nodules reach the surface and have undergone significant degassing, the degassing mechanism has evolved to volatile channel formation in nearly all samples (diamonds in Figure 6c).

Given their preserved framework and connected volatile pathways, the density of the nodules remains a key factor controlling their ascent. Density calculations reveal that, even without volatile exsolution, the maximum density of the nodules remains close to neutral buoyancy; in all cases, the density contrast between nodules and carrier melt ranges from 0.18% to 1.13% (Table 1). Consequently, once detached from the mush horizon, these plagioclase-rich nodules could readily be entrained and transported by the carrier melt (Figure 7b). As nodules ascend, bubble nucleation, growth, and coalescence occur, which can lead to their disaggregation into individual crystals in the final ascent stages. However, we observe that many nodules remained intact, as their mechanical integrity and vesicle connectivity provided structural resilience (Figure 7b).

Taken together, the Gígöldur nodules illustrate how the mechanical behaviour of upper-crustal crystal mushes during ascent is controlled by the interplay between rigid crystal frameworks, interstitial melt connectivity, and volatile distribution. Rigid frameworks provide structural stability, while interconnected volatile pathways allow for degassing and relieve ascent-induced stresses. Near-neutral buoyancy further aids the transport of coherent mush fragments. The potential for mush disaggregation is strongly depth-dependent, with the uppermost levels most sus-

ceptible to bubble-driven disruption. Whether mush fragments remain coherent or break down during ascent thus depends on framework resilience and the efficiency of volatile escape (Coombs et al., 2003; Holness et al., 2019). These findings highlight that the mesoscale structure of the subsurface mush horizon is a critical factor in governing mush behaviour (Humphreys et al., 2025). While our study focuses on Gígöldur nodules, the principles demonstrated here – framework integrity and volatile escape efficiency – are readily transferable to other upper-crustal mush systems, providing a framework for interpreting mush dynamics and degassing behaviour in diverse magmatic environments. Additional factors, such as spatial variations in strain within the conduit, decompression rate, or reactive melt flow, may also influence the likelihood of disaggregation, though here we emphasise those controls directly recorded by the nodule microstructures.

4.2. What processes govern the formation and evolution of mushes beneath Gígöldur?

A key aim of this study is to decipher how the plagioclase-dominated framework of upper-crustal mushes formed by combining textural and chemical evidence. Panjasawatwong et al. (1995) demonstrated that at crustal pressures, plagioclase with anorthite contents of 85–94 mol% can only crystallise from melts with CaO/Na_2O ratios of 10–15, Ca# values of 78–90 mol%, and Al# > 30 mol%. In contrast, the Gígöldur matrix glasses show systematically lower values for all these parameters (CaO/Na_2O = 4–7.6, Ca# = 68.8–80.8 mol%, Al# = 22.8–27.1 mol%; Table 2). These compositional contrasts imply that the high-An plagioclase cores (Figure 8) could not have crystallised from the carrier melts sampled at Gígöldur (e.g., Neave et al., 2014b). Instead, they likely represent recycled components derived from deeper, more primitive parts of the magmatic system, subsequently reworked into

shallower mushy magma reservoirs where they developed rims in equilibrium with resident melts (Figure 3e-j). We cannot directly determine the crystallisation depth of these cores from the available data, but Icelandic studies show that high-An plagioclase can form across a range of middle- to lower-crustal levels (e.g., Hansen and Grönvold, 2000; **?**; Neave et al., 2014b, 2017), so their exact origin in the system remains unconstrained. The narrow range of core compositions is consistent with derivation from a single, more primitive environment rather than incremental crystallisation at multiple crustal levels. Once these crystals were available, rim overgrowth in shallower reservoirs would have been kinetically favoured over the nucleation of new plagioclase (**?**), preserving the homogeneity of the cores while allowing the rims to capture later interactions with more evolved melts. This recycling interpretation is consistent with the expectation that high-An plagioclase is neutrally buoyant only at elevated pressures (Lange et al., 2013), allowing deep crystals to be mechanically redistributed into shallower mush zones.

Our observations and calculations allow us to place some first-order constraints on the vapour content of Icelandic mushes in the crust. Estimated maximum CO_2 concentrations of 1120–1350 ppm (Supplementary Table 4) yield saturation pressures of 1.97–2.80 kbar (Table 2) for melts contained in the mushes beneath Gígöldur, using the volatile saturation model of Iacono-Marziano et al. (2012), implemented in the VESIcal Python package (Iacovino et al., 2021). These saturation pressures straddle magma storage pressures estimated by OPAM barometry ($\sim 2.45 \pm 1.14$ kbar; Figure 5), indicating that the mushes beneath Gígöldur likely contained small but significant volumes of CO_2-rich vapour. Similar vapour-bearing mushes have been inferred beneath Bárðarbunga from seismic observations (Hudson et al.,

2017).

We therefore suggest that the Gígöldur magma was sourced from a mushy magma reservoir that formed through sill intrusion into the country rock, with mushes forming preferentially along sill boundaries (Maclennan, 2019). Intruding magma likely entrained high-An plagioclase cores that originated in deeper and compositionally distinct reservoirs and incorporated them into the present reservoir (Figure 7a; Halldorsson et al., 2008; Neave et al., 2014b). Within this mushy magma reservoir, recycled cores developed rim overgrowth while olivine and clinopyroxene co-crystallised (e.g., van Gerve et al., 2020). Density-driven segregation of these phases likely produced a plagioclase-rich roof and a mafic-rich base (e.g., Holness et al. (2019); Figure 7c). The zoning patterns observed between adjacent grains, which sometimes vary markedly (Figure 3e-j), indicate that the crystals did not share a single, uniform growth history and suggest that they were incorporated into clusters at different times and experienced differing degrees of (re-)equilibration with the resident melt (e.g., Streck, 2008; Bennett et al., 2019; van Gerve et al., 2020). Despite this variability, the compositional similarity between carrier and interstitial melts (Supplementary Figure B4) indicates that at least the final rim growth occurred in relatively homogeneous melts. Oscillatory zoning in several grains reflects non-steady-state growth driven by dynamic processes, such as convection, melt replenishment, and interface kinetics (e.g., Ginibre et al., 2002), as well as thermodynamic fluctuations in pressure, temperature, and melt composition during decompression and magma mixing (e.g., Ustunisik et al., 2014). Although the preserved melt limits direct constraints, these patterns record transient conditions during mush evolution. At the final stage of mush assembly, tex-

tural observations (Figure 3a–d,Figure 4a; more figures provided in Subbaraman et al., 2025b,c) indicate that olivine and clinopyroxene crystallised interstitially within a plagioclase framework (Figure 7c). The outermost plagioclase rims grew in equilibrium with these interstitial melts, within analytical and model uncertainties (Figure 7c, Figure 8), which were multiply saturated with the mafic phases and plagioclase (Figure 5). Continued interstitial crystallisation of mafic phases and rim overgrowth of plagioclase would have increased mush density toward neutral buoyancy, consistent with our density calculations (Table 1).

Although more detailed geochemical and isotopic measurements would be required to test our model rigorously, our observations support the view that the mushes beneath Gígöldur experienced recycling of deep high-An plagioclase cumulates that were transported to shallower levels, where they were overgrown within a shallower mushy magma reservoir. The Gígöldur nodules thus represent a small-scale analogue of plagioclase-rich environments (e.g., anorthosites, troctolites) which have been proposed to produce plagioclase-ultraphyric basalts across Iceland (e.g., Hansen and Grönvold, 2000; Neave et al., 2014b). Moreover, comparable plagioclase-rich mush zones are recognised beneath various mid-ocean ridge and ocean island settings, where they play a crucial role in the generation of diverse plagioclase-rich basalts (e.g., Cullen et al., 1989; Lange et al., 2013). Studying these plagioclase-rich mushes therefore enhances our understanding of how crystal cargoes in basaltic magmas form more generally, through processes of mush entrainment and syn-eruptive disaggregation driven by volatile exsolution and degassing.

5. Conclusions

This study examines the factors controlling the structural integrity of gabbroic nodules during magma ascent and explores the insights they provide into the structure and evolution of upper crustal (6–10 km) mushy magma reservoirs. Gabbroic nodules preserve evidence of recycled high-An plagioclase cores enclosed in lower-An rim, reflecting localised in situ modification within the mushy magma reservoir, and density-driven segregation of roof cumulates. Oscillatory zoning and variable rim patterns indicate that crystals experienced non-steady-state growth (e.g., Ginibre et al., 2002; Ustunisik et al., 2014) and were incorporated into clusters at different times. The final stage of mush assembly likely involved plagioclase rim overgrowth coupled with interstitial mafic co-crystallisation, with much of this final mush evolution occurring in relatively homogeneous melts. Volatile saturation pressure estimates indicate that the melts hosting mush fragments that ultimately erupted as gabbroic nodules were likely volatile-saturated at their final storage conditions. Despite degassing-induced stresses, the rigid crystal frameworks of erupted gabbroic nodules maintained their structural integrity, while interconnected volatile networks provided efficient degassing pathways (e.g., Coombs et al., 2003; Holness et al., 2019). Positive to neutral buoyancy likely facilitated nodule transport, allowing many nodules to remain intact and preserve primary mesoscale mush textures during ascent. In cases where bubble connectivity was poor, complete disaggregation did sometimes occur (e.g., Hansen and Grönvold, 2000), generating a plagioclase-phyric crystal cargo akin to those erupted in plagioclase-ultraphyric basaltic eruptions (e.g., Cullen et al., 1989; Lange et al., 2013; Neave et al., 2014b).

Our observations highlight general principles governing mush behaviour in active upper-crustal mush systems. The interplay of rigid crystal frameworks, melt connectivity, and vesicle network geometries governs whether mushes remain cohesive or disaggregate into crystal cargoes. Similar observations have been well documented in other crustal systems: relationships between frameworks and interstitial melt have been argued to regulate mush disaggregation in samples from mid- to lower-crustal oceanic core complexes (e.g., Boulanger et al., 2024); mush remobilisation has been invoked to explain the steady supply of macrocrysts to long-lasting Icelandic eruptions (e.g., Neave et al., 2017); resorption, clustering, and partial disaggregation have been seen to reflect complex magmatic histories in basalts from Tenerife (e.g., Horn et al., 2022); and recharge-driven remobilisation has been noted to deliver crystal cargoes in diverse arc systems (e.g., Cooper and Kent, 2014). Together, these examples reinforce the three-phase (crystal–melt–vapour) nature of mush zones, with framework rigidity, melt connectivity, and volatile distribution imposing important controls over magma storage, remobilisation, and eruptive behaviour.

CRediT authorship contribution statement

Rahul Subbaraman: Conceptualisation, Methodology, Software, Investigation, Formal analysis, Data curation, Validation, Visualisation, Writing – original draft, Writing – review & editing, Funding acquisition. **Margaret E. Hartley:** Conceptualisation, Resources, Supervision, Writing – review & editing. **Jonathan Fellowes:** Investigation. **Margherita Polacci:** Resources, Writing – review & editing. **Barbara Bonechi:** Methodology, Writing – review & editing. **Lucia Pappalardo:** Investigation, Resources. **Gianmarco Buono:** Investigation, Re-

sources, Writing – review & editing. **David A. Neave:** Conceptualisation, Supervision, Resources, Writing – review & editing.

Acknowledgements

This publication results from work carried out under Trans-National Access action under the support of EXCITE - EC - HORIZON 2020 - INFRAIA 2020 Integrating Activities for Starting Communities under grant agreement N.101005611. Part of the EPMA data acquisition was conducted during the NERC Advanced Training Short Course in Quantitative X-ray Microanalysis in Earth and Environmental Sciences, funded by NERC grant NE/Y00373X/1. RS acknowledges support from the UoM FSE Dean's Doctoral Scholarship. DAN acknowledges support from NE/T011106/1. MEH acknowledges support from NERC grant NE/P002331/1. MP and BB acknowledge support from UKRI grant 4DVOLC (MR/V023985/1). RS thanks Lee Paul and David Oliver for their support with sample preparation. Finally, we thank Martin Mangler and Bruno Scaillet for their detailed and encouraging reviews, and Chiara Maria Petrone for editorial handling.

Declaration of AI-assisted technologies in the writing process

During the preparation of this manuscript, the author(s) used ChatGPT (OpenAI) to enhance the clarity and readability of the text. The author(s) reviewed, edited, and verified all content and take full responsibility for the published work.

Supplementary materials

The following supplementary materials are available in connection with this article:

1. `MMC 1. Supplementary Information.pdf` – Contains supplementary methods, figures, and tables referenced in the main text.

2. `MMC 2. EPMA Setup + Sec Std.xlsx` – EPMA instrument settings and chemical analyses of secondary standards.

3. `MMC 3. EPMA Data - Glass + Minerals.xlsx` – Chemical analyses of matrix glasses, melt inclusions, and median mineral data used for thermobarometry and density calculations.

4. `MMC 4. Literature H2O-CO2.xlsx` – Compilation of Icelandic literature data for H_2O and CO_2 used in this study.

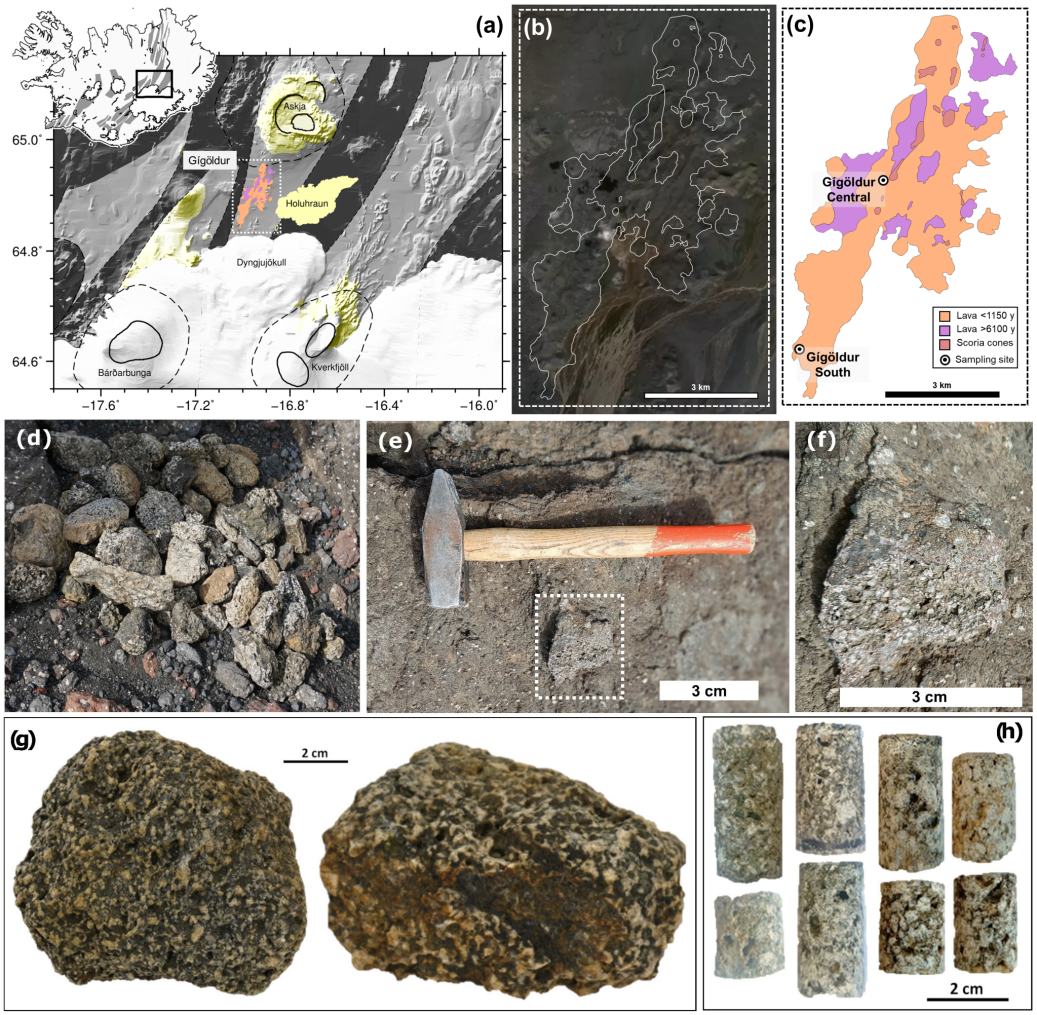

Figure 1: Geological context of gabbroic nodules. (a) Map of the highlands north of Vatnajökull showing Gígöldur, Holuhraun, Askja and Bárðarbunga. The inset shows Iceland with neovolcanic zones highlighted, with the black bold rectangle corresponding to the highlands map. Within the highlands map, the white dashed rectangle marks the area expanded in panels (b)–(c). (b) Satellite image of Gígöldur and surrounding areas from Google Earth Pro (2025), with lithological boundaries after Sigurgeirsson et al. (2015). (c) Geological map of Gígöldur showing lava flows, scoria cones, and sampling locations (modified after Sigurgeirsson et al. 2015). (d) Field photograph illustrating the compositional and textural variability of nodules collected at Gígöldur Central. (e) Gabbroic nodule observed *in situ* within plagioclase-phyric scoriaceous agglutinates. (f) Enlarged view of the nodule shown in (e). (g) Nodules used in this study: GO19-01a.X (left) and GO19-02.X (right). (h) Rock cores extracted from the two nodules: GO19-01a.X (left) and GO19-02.X (right).

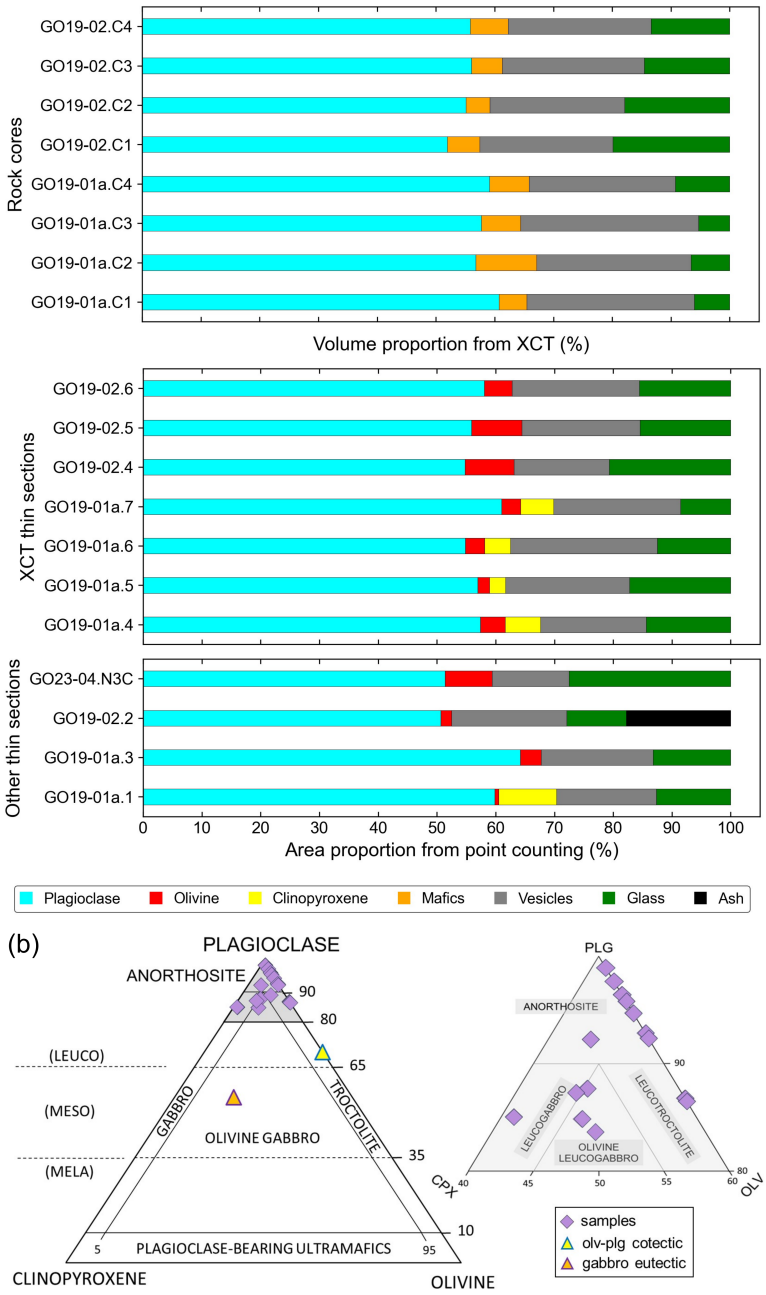

Figure 2: Phase proportions and classification of nodules. (a) Volume proportions from X-ray computed tomography (XCT) compared with area proportions from point counting. (b) IUGS gabbroic rock classification in plagioclase–olivine–clinopyroxene ternary diagrams. The main diagram shows compositional fields, the gabbro eutectic (orange triangle), and olivine–plagioclase cotectic (yellow triangle) compositions. The inset diagram enlarges the plagioclase-rich field (>80 vol%), illustrating the distribution of the studied thin sections.

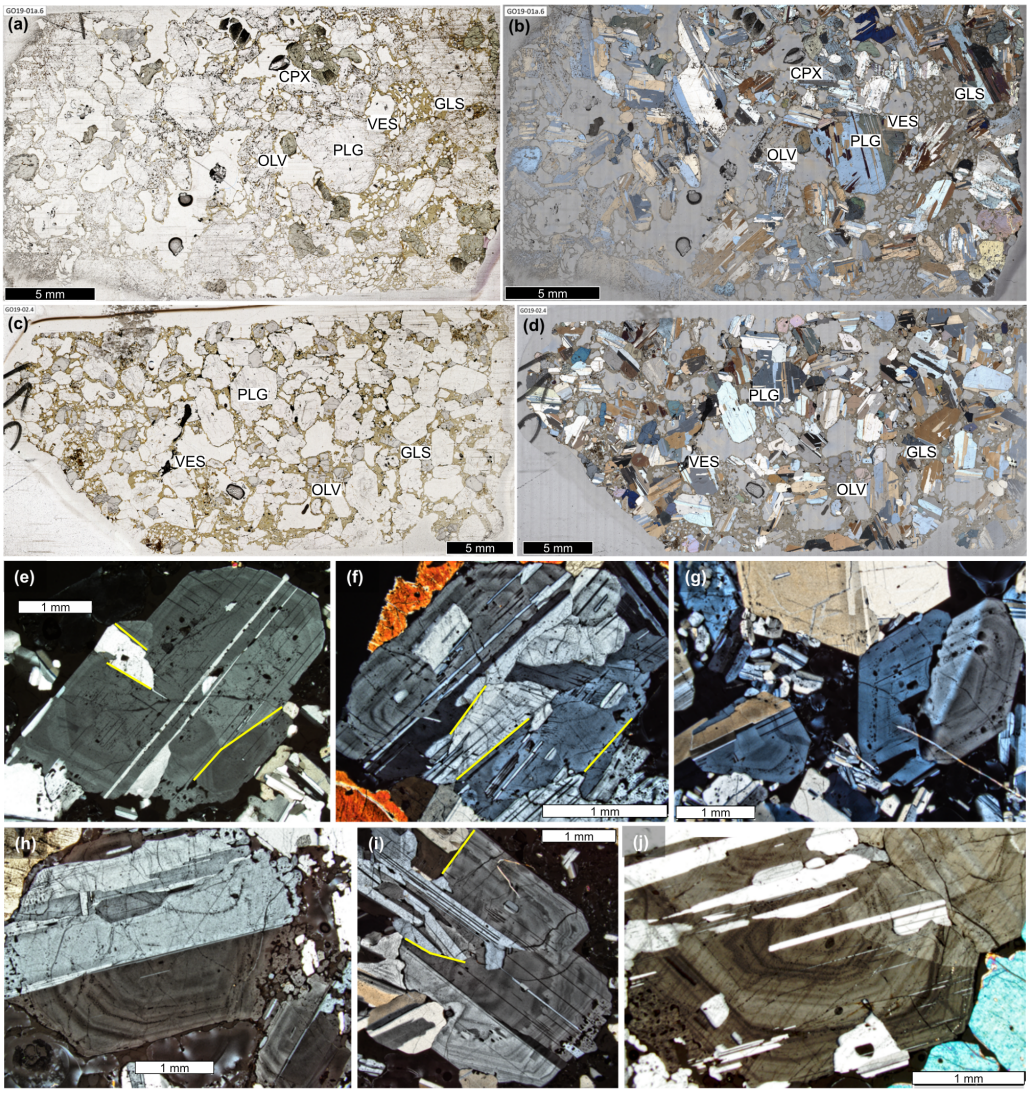

Figure 3: Petrography of gabbroic nodule thin sections. (a, c) Whole thin-section photomicrographs of samples GO19-01a.X and GO19-02.X in plane-polarised light (PPL). (b, d) Corresponding images in partial cross-polarised light (PXPL; polariser–analyser at 45°), with major phases indicated. The black scale bar represents 5 mm. CPX = clinopyroxene, GLS = matrix glass, OLV = olivine, PLG = plagioclase, VES = vesicles. (e–j) Photomicrographs of plagioclase grains from various samples showing complex zonation patterns, with multiple compositional bands enclosing both individual crystals and crystal clusters. Yellow lines mark examples of extensive grain–grain contact areas (see subsection 4.1); white scale bar represents 1 mm.

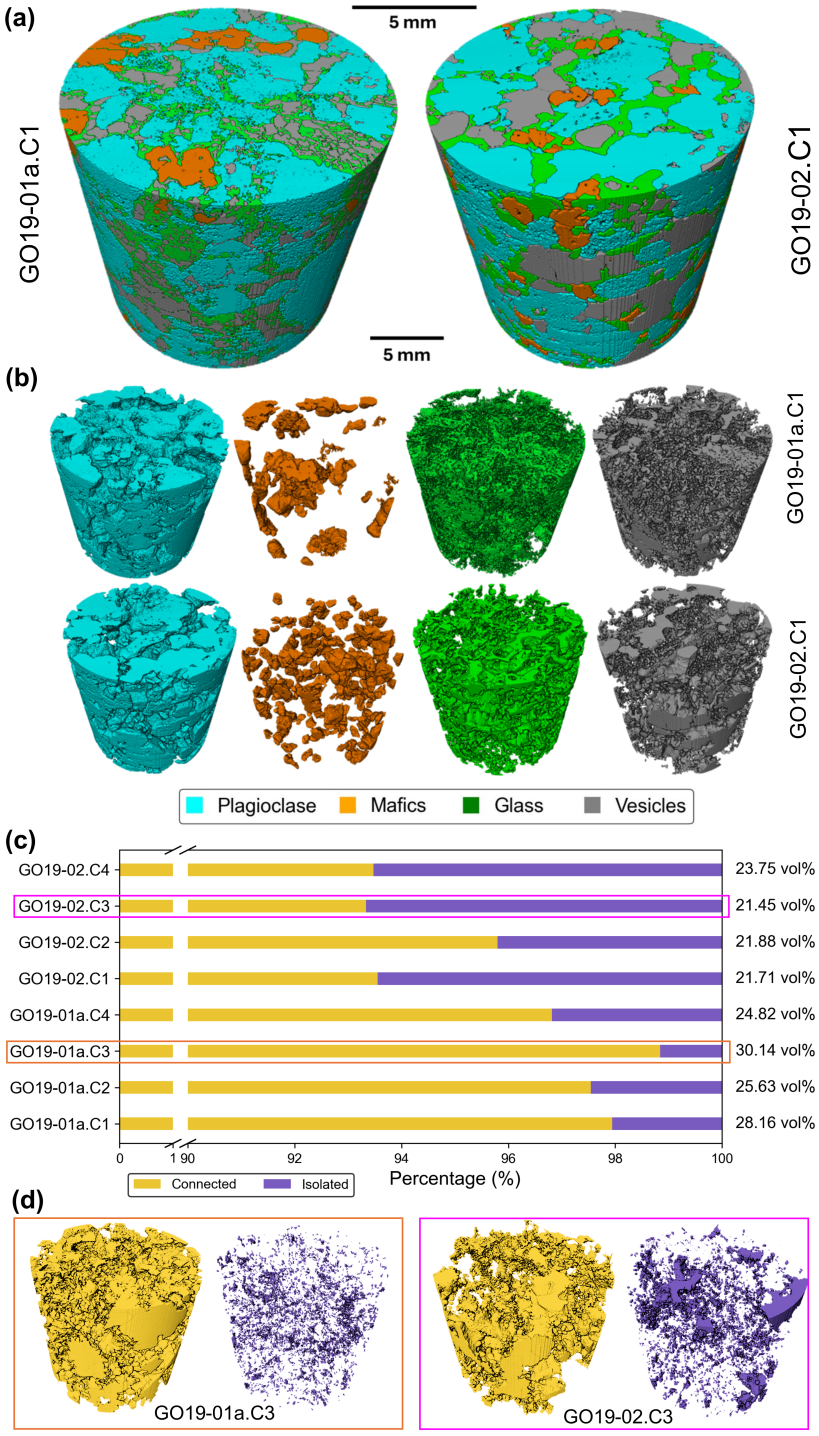

Figure 4: Results of XCT analysis. (a) Representative 3D reconstructions of whole cores with all phases combined (GO19-01a.C1 and GO19-02.C1). (b) Representative 3D reconstructions with individual phases distinguished (see legend for colour scheme). (c) Stacked bar chart showing vesicle connectivity categories (Connected and Isolated); vesicularity values for each sample are annotated on the right. The core with the highest proportion of Connected vesicles (GO19-01a.C3) is outlined in orange, and the core with the lowest proportion (GO19-02.C3) is outlined in magenta. (d) 3D reconstructions of Connected and Isolated vesicles for GO19-01a.C3 and GO19-02.C3, shown with orange and magenta outlines, respectively.

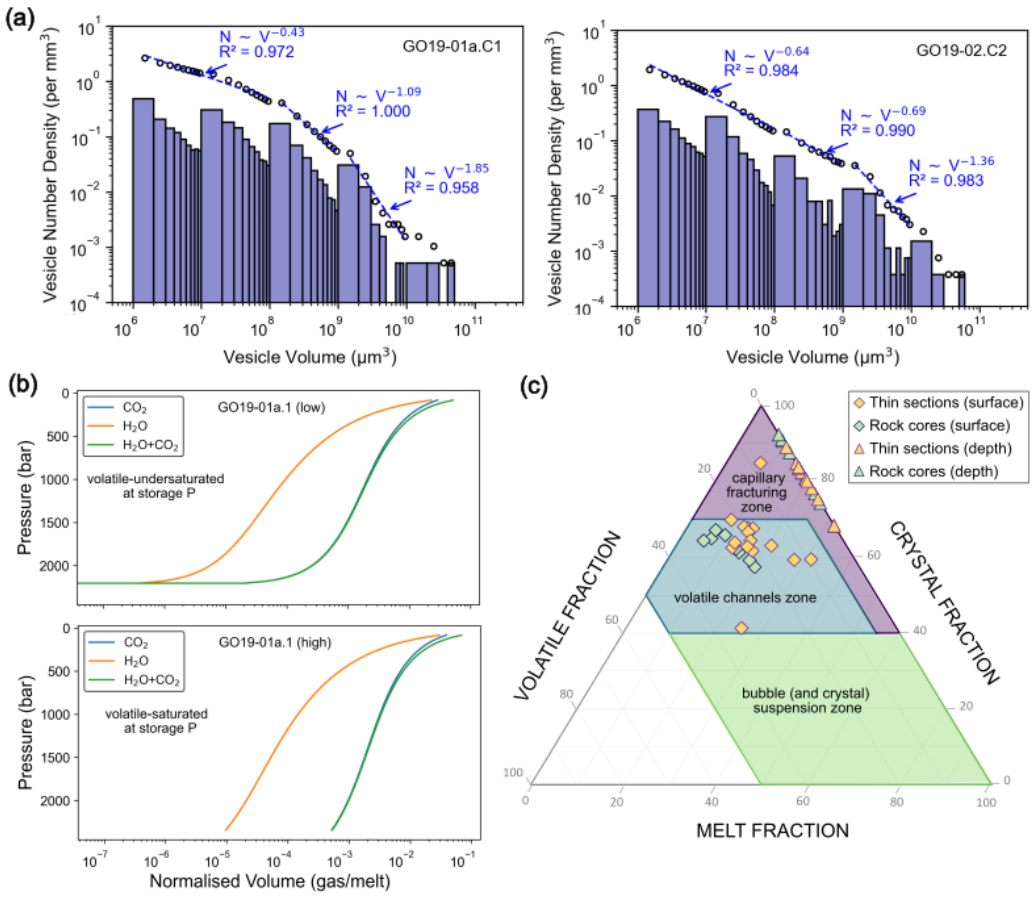

Figure 5: OPAM thermobarometry results for Gígöldur gabbroic nodules based on matrix glass compositions (Higgins and Stock, 2024). Violin plots show frequency distributions of calculated equilibrium pressures and equivalent storage depths for each sample. The number of glass analyses and median temperatures are annotated above each plot; median pressures and depths are indicated alongside each violin plot. Sample GO19-01a.1 yielded only one OPAM-saturated analysis and is shown as a single point rather than a distribution.

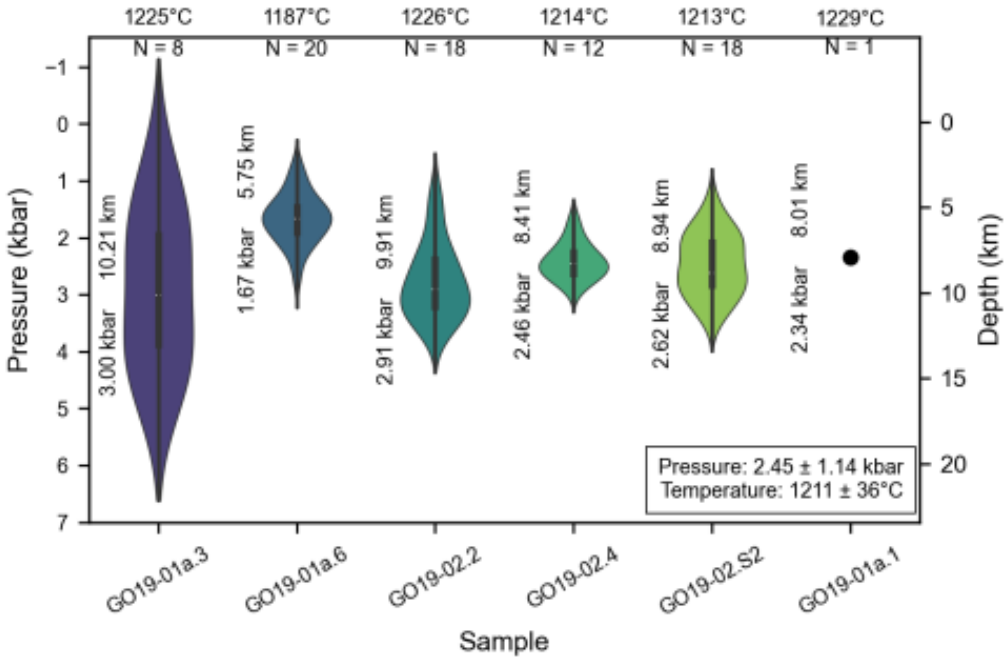

Figure 6: Vesicle growth dynamics and volatile degassing. (a) Cumulative (circles) and non-cumulative (bars) vesicle size distributions for representative cores from Batch I and Batch II, with fitted power-law trends; largest vesicles with exponents >1. (b) Closed-system degassing profiles using the model of Iacono-Marziano et al. (2012), showing CO_2, H_2O, and H_2O+CO_2 from depth of final storage (~ 2.5 kbar) to ~84.5 bar (eruption beneath Icelandic glacial ice; Hubbard et al., 2006). The upper panel illustrates a degassing melt initially undersaturated in volatiles (initial X_{H_2O} = 0.907), while the lower panel illustrates a degassing melt initially saturated in volatiles (initial X_{H_2O} = 0.88). Initial volatile contents and saturation pressures are provided in Table 2. A full set of plots is provided in the supplementary material. (c) Ternary diagram of degassing regimes (Degruyter et al., 2019): (1) bubble/crystal suspension at high melt fractions (green), (2) volatile channels at moderate melt and high crystal fractions (blue), (3) capillary fracturing at very low melt fractions (purple). At final storage conditions, assuming negligible vesicle volumes, Gígöldur samples mostly plot in the capillary fracturing zone (triangles). At near-surface conduit conditions, the same samples plot in the volatile channels zone (diamonds).

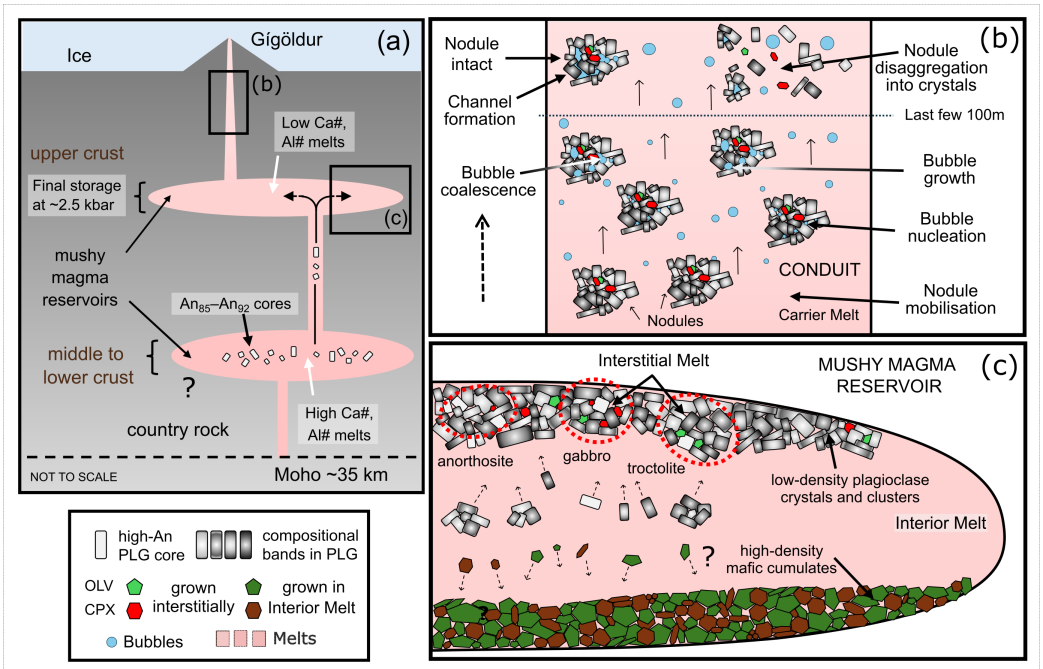

Figure 7: Conceptual schematic for the evolution, transport, and eruption of gabbroic nodules within the active mush system beneath Gígöldur. (a) Schematic plumbing system showing a deeper, compositionally more primitive reservoir of uncertain depth feeding a shallow mushy magma reservoir stored at ~2.5 kbar. High-anorthite (An_{85}–An_{92}) plagioclase cores are interpreted to have crystallised in this deeper part of the system from high-Ca#, high-Al# melts before being redistributed into the shallower upper-crustal reservoir, where they acquired overgrowth rims in equilibrium with lower-Ca#, lower-Al# melts. (b) Nodule behaviour during conduit ascent. Nodules are entrained by the carrier melt, while decompression drives bubble nucleation, growth, and coalescence. A combination of a strong crystal framework and interconnected bubble networks allows some nodules to remain intact, whereas the absence of either promotes their disaggregation into individual crystals in the upper conduit that feeds into the crystal cargo of plagioclase-ultraphyric basalts. (c) Organisation of the shallow mushy magma reservoir. Density-driven stratification produces a mafic cumulate base and a roof of recycled high-An cores modified by rim growth. Under conditions of multiple saturation, plagioclase, olivine, and clinopyroxene crystallise together from the interstitial melts. The resulting assemblages have gabbroic or troctolitic phase proportions within a plagioclase framework. The nodules erupted at the surface represent small-scale fragments of this plagioclase-dominated mush. CPX = clinopyroxene, OLV = olivine, PLG = plagioclase.

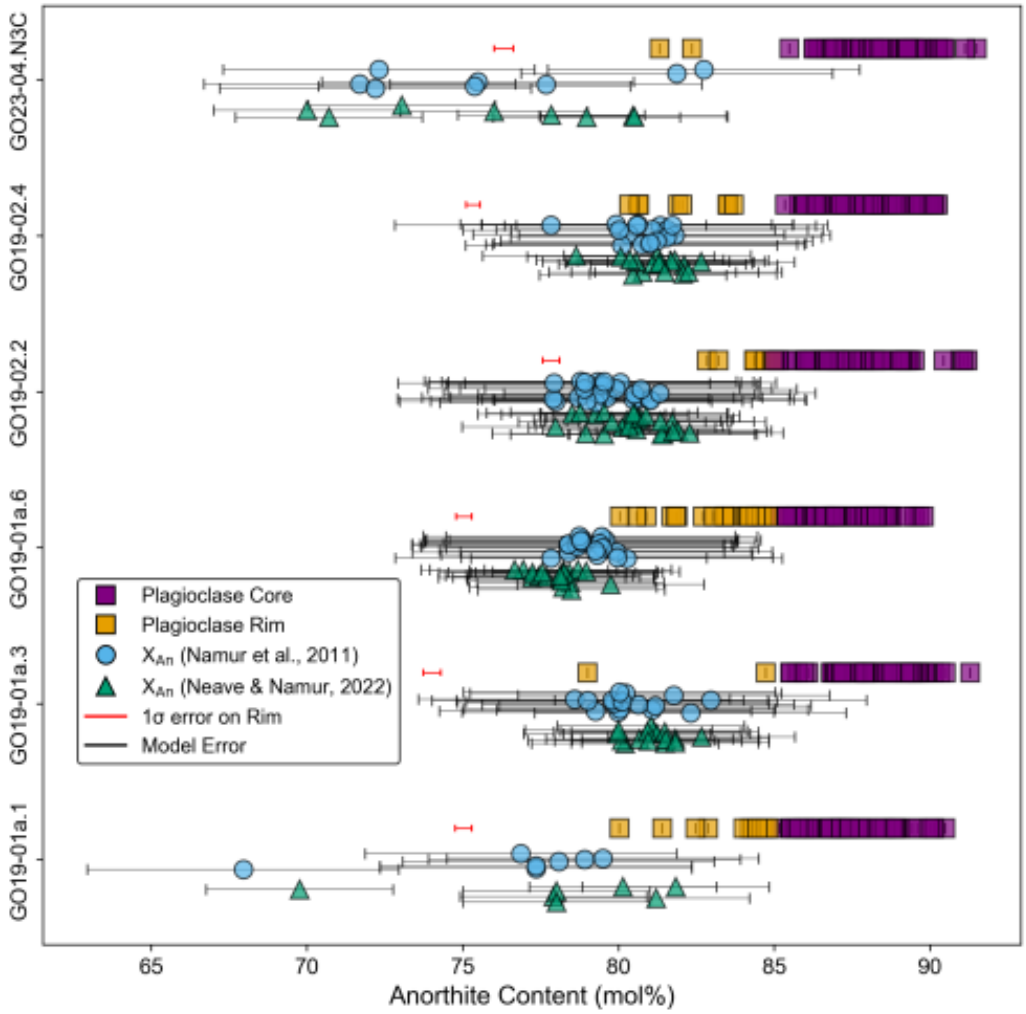

Figure 8: Anorthite contents of plagioclase cores and rims compared with equilibrium plagioclase calculations for the matrix glasses. Plagioclase cores (purple squares) are far from equilibrium with the surrounding matrix glass, indicating early crystallisation. Rims (orange squares) with the lowest An contents are in equilibrium with the surrounding matrix glass within model uncertainties. Equilibrium XAn of the matrix glass was calculated using two models: Namur et al. (2011) (blue circles) and Neave and Namur (2022) (green triangles). Horizontal red error bars indicate the mean uncertainty for rim compositions, while model error bars represent ±3–5 mol% uncertainty in the calculated equilibrium compositions.

Table 1: Phase densities, modal proportions, and bulk nodule densities for gabbroic nodules. Phase proportions are based on point counting, and densities are calculated at the final storage pressure and temperature. Nodule matrix glass is treated as interstitial melt (IM), while scoria matrix glass is treated as the carrier melt (CM). Abbreviations: PLG = plagioclase, OLV = olivine, CPX = clinopyroxene, IM = interstitial melt, CM = carrier melt.

Sample	Phase density (g/cm^3)				Vesicle-free proportions (%)				Final density (g/cm^3)		
	PLG	OLV	CPX	IM	PLG	OLV	CPX	IM	Nodule	CM	Δ_{rel}
GO19-01a.1	2.696	3.322	3.000	2.694	72.09	0.81	11.85	15.25	2.737	2.726	+0.40%
GO19-01a.3	2.701	3.253	-	2.734	79.23	4.42	-	16.35	2.731	2.736	-0.18%
GO19-01a.6	2.696	3.316	3.002	2.713	73.11	4.38	5.89	16.62	2.744	2.725	+0.69%
GO19-02.2	2.699	3.261	-	2.736	80.81	2.98	-	16.21	2.722	2.735	-0.48%
GO19-02.4	2.700	3.253	-	2.730	65.38	9.95	-	24.67	2.762	2.731	+1.13%
GO23-04.N3C	2.700	3.255	-	2.733	59.13	9.21	-	31.66	2.762	2.731	+1.13%

Table 2: Calculated melt volatile content and measured melt chemistry of nodule samples. P_{OPAM} and T_{OPAM} are calculated using OPAM thermobarometry. CO_2^{ll} and CO_2^{ul} are the lower (1020 ppm) and upper (1350 ppm) limits of the maximum CO_2 range calculated, respectively. P_{sat}^{ll} and P_{sat}^{ul} are volatile saturation pressures corresponding to mixed H_2O–CO_2 fluids with CO_2^{ll} and CO_2^{ul}, respectively. Ca# [100×Ca/(Ca+Na)], and Al# [100×Al/(Al+Si)] reflect melt chemistry relevant to the crystallisation of high-An plagioclase.

Sample	P_{OPAM} (kbar)	T_{OPAM} (°C)	H_2O (wt%)	CO_2^{ll} (ppm)	P_{sat}^{ll} (kbar)	CO_2^{ul} (ppm)	P_{sat}^{ul} (kbar)	CaO/Na_2O		Ca#		Al#	
								min	max	min	max	min	max
GO19-01a.1	2.34	1229	0.407	1020	2.22	1350	2.80	4.0	7.4	68.8	80.4	24.0	25.0
GO19-01a.3	3.00	1225	0.415	1020	2.05	1350	2.58	6.5	7.3	78.1	80.1	25.2	27.0
GO19-01a.6	1670	1187	0.398	1020	2.09	1350	2.64	5.6	7.0	75.4	79.3	24.8	26.3
GO19-02.2	2.91	1226	0.447	1020	1.97	1350	2.49	6.0	7.6	76.9	80.8	25.1	26.3
GO19-02.4	2.46	1214	0.432	1020	2.03	1350	2.56	6.2	7.5	77.5	80.5	25.4	26.4
GO23-04.N3C	2.45	1211	0.383	1020	2.06	1350	2.60	5.1	7.2	73.7	80.0	22.8	27.1

References

Annen, C., Blundy, J.D., Sparks, R.S.J., 2005. The Genesis of Intermediate and Silicic Magmas in Deep Crustal Hot Zones. Journal of Petrology 47, 505–539. doi:https://doi.org/10.1093/petrology/egi084.

Bacon, C.R., 1986. Magmatic inclusions in silicic and intermediate volcanic rocks. Journal of Geophysical Research: Solid Earth 91, 6091–6112. doi:10.1029/jb091ib06p06091.

Bai, L., Baker, D.R., Rivers, M., 2008. Experimental study of bubble growth in Stromboli basalt melts at 1 atm. Earth and Planetary Science Letters 267, 533–547. doi:10.1016/j.epsl.2007.11.063.

Bali, E., Hartley, M.E., Halldórsson, S.A., Gudfinnsson, G.H., Jakobsson, S., 2018. Melt inclusion constraints on volatile systematics and degassing history of the 2014-–2015 Holuhraun eruption, Iceland. Contributions to Mineralogy and Petrology 173. doi:10.1007/s00410-017-1434-1.

Bamber, E.C., La Spina, G., Arzilli, F., Polacci, M., Mancini, L., de' Michieli Vitturi, M., Andronico, D., Corsaro, R.A., Burton, M.R., 2024. Outgassing behaviour during highly explosive basaltic eruptions. Communications Earth and Environment 5. doi:10.1038/s43247-023-01182-w.

Bennett, E.N., Lissenberg, C.J., Cashman, K.V., 2019. The significance of plagioclase textures in mid-ocean ridge basalt (Gakkel Ridge, Arctic Ocean). Contributions to Mineralogy and Petrology 174. doi:10.1007/s00410-019-1587-1.

Bergantz, G.W., Schleicher, J.M., Burgisser, A., 2015. Open-system dynamics

and mixing in magma mushes. Nature Geoscience 8, 793–796. doi:10.1038/ngeo2534.

Berman, R.G., 1988. Internally-Consistent Thermodynamic Data for Minerals in the System Na2O-K2O-CaO-MgO-FeO-Fe2O3-Al2O3-SiO2-TiO2-H2O-CO2. Journal of Petrology 29, 445–522. doi:10.1093/petrology/29.2.445.

Bonechi, B., Bamber, E.C., Polacci, M., Arzilli, F., La Spina, G., Biagioli, E., Romero, J.E., Hazemann, J.L., Brooker, R., Atwood, R., Burton, M., 2025. Linking eruptive style with pore network geometry in tephritic/basanitic tephra from the 2021 Tajogaite eruption (Canary Islands, Spain). Bulletin of Volcanology 87. doi:10.1007/s00445-025-01833-0.

Boulanger, M., Godard, M., Ildefonse, B., Bakouche, M., 2024. Petrological Evidence for Prominent Melt-Mush Reactions During Slow-Spreading Oceanic Accretion. Geochemistry, Geophysics, Geosystems 25. doi:10.1029/2023gc011409.

Candela, P.A., 1991. Physics of aqueous phase evolution in plutonic environments. American Mineralogist 76, 1081–1091.

Cashman, K.V., Mangan, M.T., 2014. A century of studying effusive eruptions in Hawaii. Professional Paper. doi:10.3133/pp18019.

Cashman, K.V., Sparks, R.S.J., Blundy, J.D., 2017. Vertically extensive and unstable magmatic systems: A unified view of igneous processes. Science 355. doi:10.1126/science.aag3055.

Chamberlain, K.J., Barclay, J., Preece, K.J., Brown, R.J., Davidson, J.P., 2019. Lower Crustal Heterogeneity and Fractional Crystallization Control Evolution

of Small-volume Magma Batches at Ocean Island Volcanoes (Ascension Island, South Atlantic). Journal of Petrology 60, 1489–1522. doi:10.1093/petrology/egz037.

Colombier, M., Scheu, B., Wadsworth, F.B., Cronin, S., Vasseur, J., Dobson, K.J., Hess, K., Tost, M., Yilmaz, T.I., Cimarelli, C., Brenna, M., Ruthensteiner, B., Dingwell, D.B., 2018. Vesiculation and Quenching During Surtseyan Eruptions at Hunga Tonga-Hunga Ha'apai Volcano, Tonga. Journal of Geophysical Research: Solid Earth 123, 3762–3779. doi:10.1029/2017jb015357.

Coombs, M.L., Eichelberger, J.C., Rutherford, M.J., 2003. Experimental and textural constraints on mafic enclave formation in volcanic rocks. Journal of Volcanology and Geothermal Research 119, 125–144. doi:10.1016/s0377-0273(02)00309-8.

Cooper, K.M., Kent, A.J.R., 2014. Rapid remobilization of magmatic crystals kept in cold storage. Nature 506, 480–483. doi:10.1038/nature12991.

Cullen, A., Vicenzi, E., McBirney, A., 1989. Plagioclase-ultraphyric basalts of the galapagos archipelago. Journal of Volcanology and Geothermal Research 37, 325–337. doi:10.1016/0377-0273(89)90087-5.

Degruyter, W., Parmigiani, A., Huber, C., Bachmann, O., 2019. How do volatiles escape their shallow magmatic hearth? Philosophical Transactions of the Royal Society A: Mathematical, Physical and Engineering Sciences 377, 20180017. doi:10.1098/rsta.2018.0017.

Edmonds, M., Cashman, K.V., Holness, M., Jackson, M., 2019. Architecture and dynamics of magma reservoirs. Philosophical Transactions of the Royal

Society A: Mathematical, Physical and Engineering Sciences 377, 20180298. doi:https://doi.org/10.1098/rsta.2018.0298.

Edmonds, M., Wallace, P.J., 2017. Volatiles and Exsolved Vapor in Volcanic Systems. Elements 13, 29–34. doi:10.2113/gselements.13.1.29.

Gaonac'h, H., Lovejoy, S., Stix, J., Scherzter, D., 1996. A scaling growth model for bubbles in basaltic lava flows. Earth and Planetary Science Letters 139, 395–409. doi:10.1016/0012-821x(96)00039-8.

van Gerve, T.D., Neave, D.A., Almeev, R.R., Holtz, F., Namur, O., 2020. Zoned Crystal Records of Transcrustal Magma Transport, Storage and Differentiation: Insights from the Shatsky Rise Oceanic Plateau. Journal of Petrology 61. doi:10.1093/petrology/egaa080.

Ginibre, C., Wörner, G., Kronz, A., 2002. Growth kinetics of plagioclase in igneous rocks: constraints from natural zoning patterns. Contributions to Mineralogy and Petrology 143, 300–315.

Google Earth Pro, 2025. Satellite imagery of Gígöldur, Iceland. https://earth.google.com/. Data provided by Maxar Technologies, CNES/Airbus.

Halldorsson, S.A., Oskarsson, N., Gronvold, K., Sigurdsson, G., Sverrisdottir, G., Steinthorsson, S., 2008. Isotopic-heterogeneity of the Thjorsa lava—Implications for mantle sources and crustal processes within the Eastern Rift Zone, Iceland. Chemical Geology 255, 305–316. doi:10.1016/j.chemgeo.2008.06.050.

Hansen, H., Grönvold, K., 2000. Plagioclase ultraphyric basalts in Iceland: the

mush of the rift. Journal of Volcanology and Geothermal Research 98, 1–32. doi:10.1016/s0377-0273(99)00189-4.

Hauri, E.H., Maclennan, J., McKenzie, D., Gronvold, K., Oskarsson, N., Shimizu, N., 2017. CO2 content beneath northern Iceland and the variability of mantle carbon. Geology 46, 55–58. doi:10.1130/g39413.1.

Higgins, O., Stock, M.J., 2024. A New Calibration of the OPAM Thermobarometer for Anhydrous and Hydrous Mafic Systems. Journal of Petrology 65. doi:10.1093/petrology/egae043.

Holness, M.B., 2018. Melt segregation from silicic crystal mushes: a critical appraisal of possible mechanisms and their microstructural record. Contributions to Mineralogy and Petrology 173. doi:10.1007/s00410-018-1465-2.

Holness, M.B., Anderson, A.T., Martin, V.M., Maclennan, J., Passmore, E., Schwindinger, K., 2007. Textures in Partially Solidified Crystalline Nodules: a Window into the Pore Structure of Slowly Cooled Mafic Intrusions. Journal of Petrology 48, 1243–1264. doi:10.1093/petrology/egm016.

Holness, M.B., Stock, M.J., Geist, D., 2019. Magma chambers versus mush zones: constraining the architecture of sub-volcanic plumbing systems from microstructural analysis of crystalline enclaves. Philosophical Transactions of the Royal Society A: Mathematical, Physical and Engineering Sciences 377, 20180006. doi:10.1098/rsta.2018.0006.

Holness, M.B., Vukmanovic, Z., Mariani, E., 2017. Assessing the Role of Compaction in the Formation of Adcumulates: a Microstructural Perspective. Journal of Petrology 58, 643–673. doi:10.1093/petrology/egx037.

Horn, E.L., Taylor, R.N., Gernon, T.M., Stock, M.J., Farley, E.M.R., 2022. Composition and Petrology of a Mush-Bearing Magma Reservoir beneath Tenerife. Journal of Petrology 63. doi:10.1093/petrology/egac095.

Hubbard, A., Sugden, D., Dugmore, A., Norddahl, H., Pétursson, H.G., 2006. A modelling insight into the Icelandic Last Glacial Maximum ice sheet. Quaternary Science Reviews 25, 2283–2296. doi:10.1016/j.quascirev.2006.04.001.

Hudson, T.S., White, R.S., Greenfield, T., Ágústsdóttir, T., Brisbourne, A., Green, R.G., 2017. Deep crustal melt plumbing of Bárðarbunga volcano, Iceland. Geophysical Research Letters 44, 8785–8794. doi:10.1002/2017gl074749.

Humphreys, M.C.S., Namur, O., Bohrson, W.A., Bouilhol, P., Cooper, G.F., Cooper, K.M., Huber, C., Lissenberg, C.J., Morgado, E., Spera, F.J., 2025. Crystal mush processes and crustal magmatism. Nature Reviews Earth amp; Environment 6, 401–416. doi:10.1038/s43017-025-00682-x.

Iacono-Marziano, G., Morizet, Y., Le Trong, E., Gaillard, F., 2012. New experimental data and semi-empirical parameterization of H2O–CO2 solubility in mafic melts. Geochimica et Cosmochimica Acta 97, 1–23. doi:10.1016/j.gca.2012.08.035.

Iacovino, K., Matthews, S., Wieser, P.E., Moore, G.M., Bégué, F., 2021. VESIcal Part I: An Open-Source Thermodynamic Model Engine for Mixed Volatile (H2O-CO2) Solubility in Silicate Melts. Earth and Space Science 8. doi:10.1029/2020ea001584.

Klug, C., Cashman, K.V., 1994. Vesiculation of May 18, 1980, Mount St. Helens magma. Geology 22, 468–472. doi:10.1130/0091-7613(1994)022<0468:VOMMSH>2.3.CO;2.

Klug, C., Cashman, K.V., 1996. Permeability development in vesiculating magmas: implications for fragmentation. Bulletin of Volcanology 58, 87–100. doi:10.1007/s004450050128.

Lange, A.E., Nielsen, R.L., Tepley, F.J., Kent, A.J.R., 2013. The petrogenesis of plagioclase-phyric basalts at mid-ocean ridges. Geochemistry, Geophysics, Geosystems 14, 3282–3296. doi:10.1002/ggge.20207.

Lange, R.L., Carmichael, I.S.E., 1990. Chapter 2. Thermodynamic properties of silicate liquids with emphasis on density, thermal expansion and compressibility. De Gruyter. p. 25–64. doi:10.1515/9781501508769-006.

Liedl, A., Buono, G., Lanzafame, G., Dabagov, S., Della Ventura, G., Hampai, D., Mancini, L., Marcelli, A., Pappalardo, L., 2019. A 3d imaging textural characterization of pyroclastic products from the 1538 ad monte nuovo eruption (campi flegrei, italy). Lithos 340–341, 316–331. URL: http://dx.doi.org/10.1016/j.lithos.2019.05.010, doi:10.1016/j.lithos.2019.05.010.

Maclennan, J., 2019. Mafic tiers and transient mushes: evidence from Iceland. Philosophical Transactions of the Royal Society A: Mathematical, Physical and Engineering Sciences 377, 20180021. doi:10.1098/rsta.2018.0021.

Mangler, M.F., Humphreys, M.C.S., Wadsworth, F.B., Iveson, A.A., Higgins, M.D., 2022. Variation of plagioclase shape with size in intermediate magmas: a

window into incipient plagioclase crystallisation. Contributions to Mineralogy and Petrology 177. doi:10.1007/s00410-022-01922-9.

Martin, V., Pyle, D., Holness, M., 2006. The role of crystal frameworks in the preservation of enclaves during magma mixing. Earth and Planetary Science Letters 248, 787–799. doi:10.1016/j.epsl.2006.06.030.

Namur, O., Charlier, B., Toplis, M.J., Vander Auwera, J., 2011. Prediction of plagioclase-melt equilibria in anhydrous silicate melts at 1-atm. Contributions to Mineralogy and Petrology 163, 133–150. doi:10.1007/s00410-011-0662-z.

Neave, D.A., Buisman, I., Maclennan, J., 2017. Continuous mush disaggregation during the long-lasting Laki fissure eruption, Iceland. American Mineralogist 102, 2007–2021. doi:10.2138/am-2017-6015ccby.

Neave, D.A., Maclennan, J., Edmonds, M., Thordarson, T., 2014a. Melt mixing causes negative correlation of trace element enrichment and CO2 content prior to an Icelandic eruption. Earth and Planetary Science Letters 400, 272–283. doi:10.1016/j.epsl.2014.05.050.

Neave, D.A., Maclennan, J., Hartley, M.E., Edmonds, M., Thordarson, T., 2014b. Crystal Storage and Transfer in Basaltic Systems: the Skuggafjöll Eruption, Iceland. Journal of Petrology 55, 2311–2346. doi:10.1093/petrology/egu058.

Neave, D.A., Namur, O., 2022. Plagioclase archives of depleted melts in the oceanic crust. Geology 50, 848–852. doi:10.1130/g49840.1.

O'Driscoll, B., Emeleus, C.H., Donaldson, C.H., Daly, J.S., 2010. Cr-spinel Seam Petrogenesis in the Rum Layered Suite, NW Scotland: Cumulate Assimilation

and in situ Crystallization in a Deforming Crystal Mush. Journal of Petrology 51, 1171–1201. doi:10.1093/petrology/egq013.

Panjasawatwong, Y., Danyushevsky, L.V., Crawford, A.J., Harris, K.L., 1995. An experimental study of the effects of melt composition on plagioclase-melt equilibria at 5 and 10 kbar: implications for the origin of magmatic high-An plagioclase. Contributions to Mineralogy and Petrology 118, 420–432. doi:10.1007/s004100050024.

Pappalardo, L., Buono, G., Fanara, S., Petrosino, P., 2018. Combining textural and geochemical investigations to explore the dynamics of magma ascent during plinian eruptions: a somma–vesuvius volcano (italy) case study. Contributions to Mineralogy and Petrology 173. URL: http://dx.doi.org/10.1007/s00410-018-1486-x, doi:10.1007/s00410-018-1486-x.

Parmigiani, A., Degruyter, W., Leclaire, S., Huber, C., Bachmann, O., 2017. The mechanics of shallow magma reservoir outgassing. Geochemistry, Geophysics, Geosystems 18, 2887–2905. doi:10.1002/2017gc006912.

Parmigiani, A., Faroughi, S., Huber, C., Bachmann, O., Su, Y., 2016. Bubble accumulation and its role in the evolution of magma reservoirs in the upper crust. Nature 532, 492–495. doi:10.1038/nature17401.

Parmigiani, A., Huber, C., Bachmann, O., Chopard, B., 2011. Pore-scale mass and reactant transport in multiphase porous media flows. Journal of Fluid Mechanics 686, 40–76. doi:10.1017/jfm.2011.268.

Paulatto, M., Moorkamp, M., Hautmann, S., Hooft, E., Morgan, J.V., Sparks, R.S.J., 2019. Vertically Extensive Magma Reservoir Revealed From Joint In-

version and Quantitative Interpretation of Seismic and Gravity Data. Journal of Geophysical Research: Solid Earth 124, 11170–11191. doi:10.1029/2019jb018476.

Polacci, M., Baker, D.R., La Rue, A., Mancini, L., Allard, P., 2012. Degassing behaviour of vesiculated basaltic magmas: an example from Ambrym volcano, Vanuatu Arc. Journal of Volcanology and Geothermal Research 233–234, 55–64. doi:10.1016/j.jvolgeores.2012.04.019.

Polacci, M., Baker, D.R., Mancini, L., Favretto, S., Hill, R.J., 2009. Vesiculation in magmas from Stromboli and implications for normal Strombolian activity and paroxysmal explosions in basaltic systems. Journal of Geophysical Research: Solid Earth 114. doi:10.1029/2008jb005672.

Proussevitch, A., Ketcham, R., Carlson, W., Sahagian, D., 1998. Preliminary results of X-ray CT analysis of Hawaiian vesicular basalts. Eos 79, 360.

Roduit, N., 2008. JMicroVision: Image analysis toolbox for measuring and quantifying components of high-definition images. https://jmicrovision.github.io.

Shea, T., Houghton, B.F., Gurioli, L., Cashman, K.V., Hammer, J.E., Hobden, B.J., 2010. Textural studies of vesicles in volcanic rocks: An integrated methodology. Journal of Volcanology and Geothermal Research 190, 271–289. doi:10.1016/j.jvolgeores.2009.12.003.

Sigurgeirsson, M.A., Árni Hjartarson, Kaldal, I., mundsson, K.S., ur Garð ar Kristinsson, S., Víkingsson, S., 2015. Geological Map of the Northern Volcanic Zone, Iceland. Southern Part.

Sparks, R.S.J., Brazier, S., 1982. New evidence for degassing processes during explosive eruptions. Nature 295, 218–220. doi:10.1038/295218a0.

Sparks, R.S.J., Cashman, K.V., 2017. Dynamic Magma Systems: Implications for Forecasting Volcanic Activity. Elements 13, 35–40. doi:10.2113/gselements.13.1.35.

Streck, M.J., 2008. Mineral textures and zoning as evidence for open system processes. Reviews in Mineralogy and Geochemistry 69, 595–622. doi:10.2138/rmg.2008.69.15.

Subbaraman, R., Buono, G., Pappalardo, L., 2025a. 3D XCT scans of 15mm gabbroic nodules from Gígöldur, Iceland. doi:10.5880/fidgeo.2025.082.

Subbaraman, R., Hartley, M., Neave, D.A., 2025b. Thin section scans of gabbro nodules, scoria, plagioclase-phyric basalt, hyaloclastite from Gígöldur, central Iceland. Figshare. doi:10.48420/28435859.v1.

Subbaraman, R., Hartley, M., Polacci, M., Bonechi, B., Pappalardo, L., Buono, G., Neave, D.A., 2025c. X-ray computed micro-tomography (XCT) 3D reconstructions of Icelandic gabbro nodules. Figshare. doi:10.48420/28431773.v1.

Toramaru, A., 2006. BND (bubble number density) decompression rate meter for explosive volcanic eruptions. Journal of Volcanology and Geothermal Research 154, 303–316. doi:10.1016/j.jvolgeores.2006.03.027.

Tukey, J.W., 1977. Exploratory Data Analysis. Addison-Wesley Pub. Co., Reading, MA.

Ustunisik, G., Kilinc, A., Nielsen, R.L., 2014. New insights into the processes controlling compositional zoning in plagioclase. Lithos 200–201, 80–93. doi:10.1016/j.lithos.2014.03.021.